ELSEVIER

Journal of Power Sources 108 (2002) 174–184

JOURNAL OF POWER SOURCES

www.elsevier.com/locate/jpowsour

Modeling the overcharge process of VRLA batteries

W.B. Gu[1], G.Q. Wang, C.Y. Wang*

Department of Mechanical and Nuclear Engineering, Electrochemical Engine Center, Pennsylvania State University, University Park, PA 16802 USA

Received 30 November 2001; accepted 2 January 2002

Abstract

A three-phase, electrochemical and thermal coupled model is developed for valve-regulated lead–acid (VRLA) batteries. Physical phenomena important to the VRLA battery overcharge process, such as gas generation, transport, and recombination, electrolyte displacement and capillary flow, and the venting event during discharge/rest/charge, are incorporated in the model. The effects of important parameters, including the electrolyte saturation level, interfacial mass transfer coefficient of oxygen, and electrode morphology factor (MF), are extensively studied. An overview of the simulation capabilities of the present comprehensive model is provided.

Keywords: VRLA battery; Overcharge; Oxygen cycle; Capillary flow; Mathematical model

1. Introduction

Valve-regulated lead–acid (VRLA) batteries are being used to power electric vehicles (EV) because of their affordability and reliability. A unique feature of the VRLA cell is its internal gas cycle in which oxygen evolved during overcharging of the positive electrode transports through a gas–pore network to the negative electrode where it is reduced [1,2]. As oxygen reactions accompany primary electrode reactions during charge, a VRLA battery needs to be overcharged to a certain extent to reach its full charge capacity. Its cycle life can be greatly affected by how it is charged [3]. While an advanced charging algorithm for VRLA batteries may be achieved through extensive laboratory testing, a comprehensive first-principle-based mathematical model promises to provide fundamental understanding of the processes involved and, thus, serve as an efficient tool to search for an optimal charging algorithm.

Prior efforts have been made to develop mathematical models for VRLA batteries to simulate their discharge and charge performance. Notably, Bernardi and Carpenter [4] presented an elegant model of oxygen evolution and recombination in a lead–acid battery. This model, however, assumes infinitely rapid transport of oxygen across the separator and, thus, the rate of oxygen recombination is limited only by the oxygen reduction kinetics on Pb electrode. As a result, the electrolyte saturation level in the separator would not affect the oxygen cycle. In addition, their model is isothermal. Newman and Tiedemann [5] discussed a lumped-parameter model that sought to clarify the oxygen evolution and recombination mechanisms. Current and species concentration distributions were ignored in order to considerably simplify their model. As a result, their model does not have resolution to ascertain the effects of transport properties and separator design on the internal gas cycle. Gu et al. [6,7] developed a comprehensive model that includes the following aspects: (1) multi-dimensionality; (2) electrochemical kinetics; (3) electrolyte flow; (4) species transport by diffusion, convection and migration; (5) variable porosity of electrodes; (6) variable electrochemical and transport properties and (7) cycling.

The objectives of this paper are to extend the lead–acid model of Gu et al. [6,7] and with particular focus on the internal oxygen cycle as well as its effects on the full charge and overcharge behaviors of VRLA batteries. Specifically, we intend to: (1) include electrolyte displacement and capillary flow; (2) account for oxygen gas transport and (3) couple the thermal process with the battery model so that one can predict both electrochemical and thermal behaviors under non-isothermal conditions. While the present effort is directed towards a single cell, the developed model framework is expected to be extendable to multi-cell modules.

* Corresponding author. Tel.: +814-863-4762; fax: +814-863-4848.
E-mail address: cxw31@psu.edu (C.Y. Wang).
[1] Present address: General Motors Global R&D, Global Alternative Propulsion Center, 10 Carriage Street, P.O. Box 603, Honeoye Falls, NY 14472-0603, USA.

0378-7753/02/$ – see front matter
PII: S0378-7753(02)00043-5

Nomenclature

a	specific surface area active for electrode reaction (cm^2/cm^3)
c^i	concentration of species i in a phase (mol/cm^3)
c_p	specific heat (J/kg K)
d_s	particle diameter (cm)
D^i	diffusion coefficient of species i (cm^2/s)
EUC	electrode utilization coefficient defined as the ratio of discharged to the maximum charge capacity
F	Faraday's constant (96,487 C/mol)
h	heat transfer coefficient (W/cm^2 K)
H'	Henry constant
$i_{0j,\mathrm{ref}}$	exchange current density of reaction j at a reference state (A/cm^2)
i_{nj}	transfer current density of reaction j (A/cm^2)
I	applied current density (A/cm^2)
$J_{\mathrm{eg}}^{\mathrm{O_2}}$	evaporation rate of oxygen at the electrolyte/gas interface (mol/cm^3 s)
k	interfacial mass transfer coefficient at the electrolyte/gas interface (cm/s)
k_{re}	relative permeability of the electrolyte phase in porous electrode or separator
K	absolute permeability of a porous medium (cm^2)
l	diffusion length
M	molecular weight (kg/kmol)
p	pressure (bar)
P_c	valve closing pressure (bar)
P_o	valve opening pressure (bar)
q	volumetric heat generation rate (J/cm^3 s)
Q	volumetric heat removal rate from the cell (J/cm^3 s)
R	universal gas constant (8.3143 J/mol K)
s	electrolyte saturation
S	source term
t	time (s)
t_+^0	transference number of hydrogen ions with respect to the solvent velocity
T	cell temperature (K)
U_j	open-circuit potential of electrode reaction j (V)
$\boldsymbol{v}_e$	electrolyte velocity vector (cm/s)
V	applied voltage (V)
V_c	cell volume (cm^3)
$\widehat{V}_e$	partial molar volume of H_2SO_4
V_g	gas volume (cm^3)
$\widehat{V}_0$	partial molar volume of H_2O

Greek symbols

α	transfer coefficient
ε	volume fraction of a phase, porosity of a porous medium
ϕ	potential in a phase (V)
γ, δ	reaction-specific constant in kinetic rate equations in Table 1
η_j	surface overpotential of electrode reaction j (V)
κ	ionic conductivity of electrolyte (S/cm)
κ_D	diffusional conductivity (A/cm)
μ	electrolyte viscosity (kg/cm s)
ρ	density (g/cm^3)
σ	conductivity of solid active material (S/cm)

Subscripts

c	capillary
e	electrolyte phase
eff	effective
eg	electrolyte/gas interface
g	gas phase
s	solid phase
se	solid/electrolyte interface
sep	separator
0	initial value

Superscripts

avg	average
eff	effective
H	proton
O_2	oxygen

2. Theory

2.1. Description of the system

As schematically shown in Fig. 1, the VRLA cell under consideration consists of a negative electrode ($Pb/PbSO_4$), a positive electrode ($PbO_2/PbSO_4$), an absorptive glass mat (AGM) separator, and a head space to store evolved gas. The electrolyte is H_2SO_4. Electrochemical reactions taking place at each electrode during charge and discharge are given as follows.

Positive electrode ($PbO_2/PbSO_4$):

$$PbSO_{4(s)} + 2H_2O \underset{\text{discharge}}{\overset{\text{charge}}{\rightleftarrows}} PbO_{2(s)} + HSO_4^- + 3H^+ + 2e^- \quad (1)$$

with oxygen evolution

$$2H_2O \rightarrow O_2 + 4H^+ + 4e^- \quad (2)$$

and hydrogen recombination

$$H_2 \rightarrow 2H^+ + 2e^- \quad (3)$$

Negative electrode ($Pb/PbSO_4$):

$$PbSO_{4(s)} + H^+ + 2e^- \underset{\text{discharge}}{\overset{\text{charge}}{\rightleftarrows}} Pb_{(s)} + HSO_4^- \quad (4)$$

with oxygen recombination

$$O_2 + 4H^+ + 4e^- \rightarrow 2H_2O \quad (5)$$

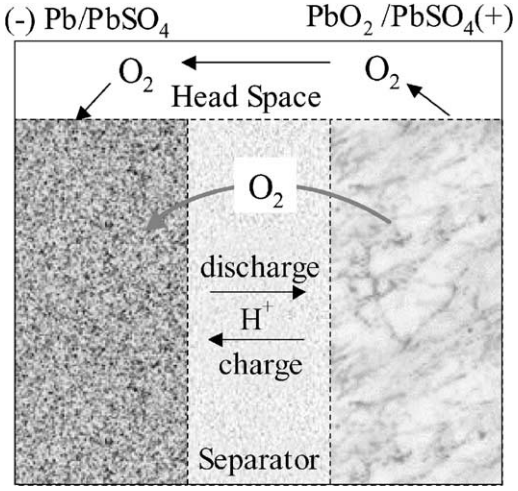

Fig. 1. Schematic of a VRLA cell and its oxygen cycle.

and hydrogen evolution

$$2H^+ + 2e^- \rightarrow H_2 \quad (6)$$

Overall cell reaction:

$$2PbSO_{4(s)} + 2H_2O \underset{\text{discharge}}{\overset{\text{charge}}{\rightleftarrows}} Pb_{(s)} + PbO_{2(s)} + 2H_2SO_4 \quad (7)$$

The side reactions (2), (3), (5) and (6) constitute the internal oxygen and hydrogen cycles in the cell. In the presence of the side reactions, a VRLA cell is a three-phase system consisting of the solid matrix, the liquid electrolyte and a gas phase. During charging and overcharging, oxygen is generated at the PbO_2/electrolyte interface and may evolve into the gas phase after exceeding its solubility limit in the electrolyte. The oxygen can then be transported, via the liquid and gas phases, from the positive to negative electrode where the oxygen gas may dissolve back in the electrolyte and be reduced at the Pb/electrolyte interface. This process forms an internal oxygen cycle in VRLA cells. Hydrogen is generated following Eq. (6) at the negative electrode when the electrode potential goes too low. Hydrogen recombination occurring at the positive electrode as described by Eq. (3) is negligible because of its poor kinetics [8,9]. Accumulation of oxygen and hydrogen in the gas phase contributes to the cell pressure build-up, thereby causing venting.

3. Model assumptions

1. A continuous gas–pore network exists in the cell for gas transport and there is a head space right above the cell with a constant volume to store excess gas. The gas obeys the ideal gas law.
2. The solid phase is completely covered by the electrolyte film. In other words, no mass transfer occurs at the active materials/gas interface.
3. Gas convection is neglected due to limited gas volume fraction inside the cell, leaving the gaseous oxygen transport by diffusion only.
4. With the exception of the dissolved oxygen species, interfacial chemical and electrical equilibrium exists in the electrolyte phase due to large values of the mass diffusivity and ionic conductivity.
5. Hydrogen recombination at the positive electrode is neglected due to its poor kinetics.

4. Mathematical formulation

4.1. Governing equations

With the above assumptions, a multiphase, electrochemical and thermal coupled model for the system considered is derived based on the modeling approach presented in [10,11]. Fig. 2 summarizes the present model formulation and its predictabilities. The battery thermal process fully couples with the electrochemical model via the heat generation rate and temperature-dependent physico-chemical properties. The derivation of the momentum equation that describes the capillary flow of the electrolyte is detailed in the Appendix A. The detailed derivation of other governing equations is similar to that for the Ni–MH battery [12] and, thus, will not be repeated here. The final model equations are summarized in Table 1, along with source terms and effective transport properties appearing in the conservation equations as listed in Tables 2 and 3, respectively. Only important parameters appearing in Section 6 are elaborated in the subsequent sections.

Electrolyte saturation: The electrolyte saturation is defined as

$$s = \frac{\varepsilon_e}{\varepsilon} = 1 - \frac{\varepsilon_g}{\varepsilon} \quad (8)$$

where ε is the porosity of an electrode or separator, ε_e and ε_g are the volume fractions of electrolyte and gas phases, respectively. Oxygen transport from the positive to negative electrode is facilitated by low saturations of electrolyte (i.e. large void volume) in the separator. Culpin and Hayman [13] showed that the effective oxygen gas diffusion coefficient could vary by three orders of magnitude if the saturation level changes from 90 to 70%. Brost [14] further documented the implication of this effect to the field performance of VRLA batteries. The electrolyte saturation, which determines the capillary pressure, is a primary driving force to the capillary flow of the electrolyte [15].

Interfacial mass transfer coefficient of oxygen: The interfacial evaporation rate of oxygen from liquid to gas phase is determined by

$$J_{eg}^{O_2} = k(c_e^{O_2} - H' c_g^{O_2}) \quad (9)$$

where k is the interfacial mass transfer coefficient of the dissolved oxygen on the electrolyte side and H' is the

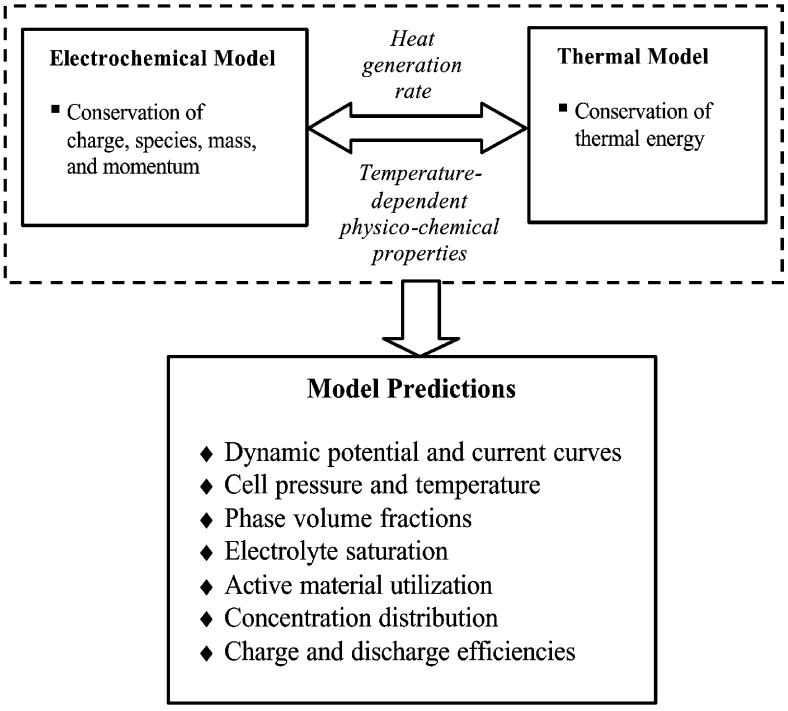

Fig. 2. The thermal-electrochemical coupled model.

Henry constant. The difference between the phase-averaged concentration, $c_e^{O_2}$, and the interfacial concentration of dissolved oxygen, $H' c_g^{O_2}$, provides a driving force for interfacial mass transfer from the electrolyte to the gas phase. Using the concept of diffusion length proposed by Wang et al. [10], the mass transfer coefficient can further be expressed as

$$k = a_{eg} \frac{D_e^{O_2}}{l_{eg}} \tag{10}$$

Table 1
Summary of governing equations

Kinetic rate equations ($\eta_j = \phi_s - \phi_e - U_j$)	Primary reactions ($j = 1$ and 4): $i_{nj} = i_{0j,ref}\left(\frac{c^H}{c_{ref}^H}\right)^{\gamma}\left[\exp\left(\frac{\alpha_{aj}F}{RT}\eta_j\right) - \exp\left(-\frac{\alpha_{cj}F}{RT}\eta_j\right)\right]$
	Oxygen generation and recombination ($j = 2$ and 5): $i_{nj} = i_{0j,ref}\left(\frac{c^H}{c_{ref}^H}\right)^{\gamma_{O_2}}\left[\exp\left(\frac{\alpha_{aj}F}{RT}\eta_j\right) - \left(\frac{c_e^{O_2}}{c_{e,ref}^{O_2}}\right)^{\delta_{O_2}}\exp\left(-\frac{\alpha_{cj}F}{RT}\eta_j\right)\right]$
	Hydrogen evolution ($j = 6$): $i_{nj} = -i_{0j,ref}\left(\frac{c^H}{c_{ref}^H}\right)^{\gamma_{H_2}}\exp\left(-\frac{\alpha_{cj}F}{RT}\eta_j\right)$
Conservation of charge	In electrolyte: $\nabla\cdot(\kappa^{eff}\nabla\phi_e) + \nabla\cdot[\kappa_D^{eff}\nabla(\ln c^H)] + S_e^c = 0$
	In solid electrode: $\nabla\cdot(\sigma^{eff}\nabla\phi_s) - S_e^c = 0$
Conservation of species	In electrolyte: $\frac{\partial(\varepsilon_e c^H)}{\partial t} + \nabla\cdot(\boldsymbol{v}_e c^H) = \nabla\cdot(D_{eff}^H\nabla c^H) + S^H$
	$\frac{\partial(\varepsilon_e c_e^{O_2})}{\partial t} + \nabla\cdot(\boldsymbol{v}_e c_e^{O_2}) = \nabla\cdot(D_{e,eff}^{O_2}\nabla c_e^{O_2}) + S_e^{O_2}$
	In gas phase: $\frac{\partial(\varepsilon_g c_g^{O_2})}{\partial t} = \nabla\cdot(D_{g,eff}^{O_2}\nabla c_g^{O_2}) + J_{eg}^{O_2}$
Conservation of mass	In electrolyte: $\frac{\partial\varepsilon_e}{\partial t} + \nabla\cdot\boldsymbol{v}_e = S_e^V$
	In solid electrode: $\frac{\partial\varepsilon_s}{\partial t} = S_s^V$
Conservation of momentum	$\boldsymbol{v}_e = -D_c\nabla s - D_{\varepsilon/K}\nabla\left(\frac{\varepsilon}{K}\right)^{1/2}$ or $\varepsilon\frac{\partial s}{\partial t} = \nabla\cdot D_c\nabla s + \nabla\cdot D_{\varepsilon/K}\nabla\left(\frac{\varepsilon}{K}\right)^{1/2} + (S_e^V + sS_s^V)$
Conservation of thermal energy	$\frac{d(\rho c_p T)}{dt} = q - Q$

Table 2
Source terms in conservation equations

Terms	Positive electrode	Separator	Negative electrode
S_e^c	$a_1 i_{n1} + a_2 i_{n2}$	0	$a_4 i_{n4} + a_5 i_{n5} + a_6 i_{n6}$
S^H	$\frac{3-2t_+^0}{2F} a_1 i_{n1} + \frac{1-t_+^0}{F} a_2 i_{n2}$	0	$\frac{1-2t_+^0}{2F} a_4 i_{n4} + \frac{1-t_+^0}{F}(a_5 i_{n5} + a_6 i_{n6})$
$S_e^{O_2}$	$\frac{1}{4F} a_2 i_{n2} - J_{eg}^{O_2}$	$-J_{eg}^{O_2}$	$\frac{1}{4F} a_5 i_{n5} - J_{eg}^{O_2}$
$J_{eg}^{O_2}$	$k(c_e^{O_2} - H' c_g^{O_2})$, $k = a_{eg} \frac{D_e^{O_2}}{l_{eg}}$,		
S_e^V	$[\widehat{V}_e(3-2t_+^0) - 2\widehat{V}_0] \frac{a_1 i_{n1}}{2F} + [\widehat{V}_e(2-2t_+^0) - \widehat{V}_0] \frac{a_2 i_{n2}}{2F}$	0	$\widehat{V}_e(1-2t_+^0) \frac{a_4 i_{n4}}{2F} + [\widehat{V}_e(2-2t_+^0) - \widehat{V}_0] \frac{a_5 i_{n5}}{2F} + \widehat{V}_e(2-2t_+^0) \frac{a_6 i_{n6}}{2F}$
S_s^V	$\left(\frac{M_{PbO_2}}{\rho_{PbO_2}} - \frac{M_{PbSO_4}}{\rho_{PbSO_4}}\right) \frac{a_1 i_{n1}}{2F}$	0	$\left(\frac{M_{PbSO_4}}{\rho_{PbSO_4}} - \frac{M_{Pb}}{\rho_{Pb}}\right) \frac{a_4 i_{n4}}{2F}$
q	$\frac{1}{V_c} \int_{V_c} a_j \sum_j \left(\eta_j + T \frac{\partial U_j}{\partial T}\right)$		
	$\mathrm{d}V \frac{1}{V_c} \int_{V_c} [\kappa^{eff} \nabla\phi_e \cdot \nabla\phi_e + \sigma^{eff} \nabla\phi_s \cdot \nabla\phi_s] \mathrm{d}V$		

where a_{eg} is the specific area of the electrolyte/gas interface, $D_e^{O_2}$ the diffusion coefficient of the dissolved oxygen in the electrolyte, and l_{eg} is the microscopic diffusion length and its value is proportional to the electrolyte film thickness [10]. Oxygen recombination at the negative electrode is limited by the interfacial mass transfer coefficient. A thin film condition in the negative electrode will facilitate the oxygen transport through the electrolyte/gas interface and, hence, the oxygen recombination.

Electrode morphology factor (*MF*): A principal geometric parameter for characterizing electrode performance is the specific area active for electrode reaction j, which is, in turn, dependent upon the porosity and particle size as well as the local state of charge (SOC), namely,

$$\begin{aligned} a_{sj} &= a_{si}(1 - \mathrm{EUC}^{\xi}), \quad \text{for discharge } i = PbO_2 \text{ or Pb} \\ a_{sj} &= a_{si}\mathrm{EUC}^{\xi}, \quad \text{for charge } i = PbO_2 \text{ or Pb} \end{aligned} \tag{11}$$

Table 3
Effective transport properties in conservation equations

Symbol	Expression	Reference
κ^{eff}	$\varepsilon_e^{1.5} \kappa$	Bruggeman relation
κ_D^{eff}	$\frac{RT\kappa^{eff}}{F}(2t_+^0 - 1)$	[6]
σ^{eff}	$\varepsilon_s^{1.5} \sigma$	Bruggeman relation
D_{eff}^H	$\varepsilon_e^{1.5} D^H$	Bruggeman relation
$D_{e,eff}^{O_2}$	$\varepsilon_e^{1.5} D_e^{O_2}$	Bruggeman relation
$D_{g,eff}^{O_2}$	$f(s) D_g^{O_2}$	empirical correlation
D_c	$-\sigma \left(\frac{\varepsilon}{K}\right)^{1/2} J'(s) \frac{K k_{re}}{\mu}$	Eq. (A.10)
$D_{\varepsilon/K}$	$-\sigma J(s) \frac{K k_{re}}{\mu}$	Eq. (A.11)
K	$\frac{\varepsilon^3 d_s^2}{180(1-\varepsilon)^2}$	Kozeny–Carman equation

for primary reactions and

$$a_{sj} = a_{si}(1 - \mathrm{EUC}^{\xi}), \quad i = PbO_2 \text{ or Pb} \tag{12}$$

for oxygen and hydrogen reactions. Here, a_s denotes the specific area, with subscript i denoting the active materials PbO_2 at the positive electrode and Pb at the negative electrode, respectively and EUC represents the electrode utilization coefficient defined as the ratio of used charge capacity to the maximum charge capacity at fully-charged state. Eqs. (11) and (12) describe the amount of active area during discharge or charge, and the exponent ξ is a MF describing the rate of change in the specific area.

Cell pressure and gas partial pressures: The average cell pressure can be calculated by summing up partial pressures of all gases present in the gas phase:

$$p_g^{avg} = \sum_i p^i, \quad i = O_2 \text{ and } N_2 \tag{13}$$

where the nitrogen gas partial pressure is determined from the initial condition and remains unchanged until venting takes place. The oxygen and hydrogen partial pressures are calculated using the ideal gas law:

$$p^i = c_g^{i,avg} RT, \quad i = O_2 \text{ and } H_2 \tag{14}$$

The average oxygen and hydrogen concentrations in the gas phase are evaluated by

$$c_g^{i,avg} = \frac{1}{V_c} \int_{V_c} \varepsilon_g c_g^i \, \mathrm{dV}, \quad i = O_2 \text{ and } H_2 \tag{15}$$

where V_c is the entire cell volume including that of the head space.

In a VRLA battery, the pressure is regulated through a venting valve. Whenever the internal gas pressure becomes greater than the valve preset opening pressure, P_o, gas is

released into the ambient until the internal pressure drops below the valve preset closing pressure, P_c. Assuming that the time of gas relief at pressures higher than the opening pressure of the valve is negligible, a single venting event can be simply modeled by the following procedure:

$$\begin{aligned} &\text{if } p_g^{avg} < P_o, \text{ then } n_g = n_g \text{ and } p_g^{avg} = p_g^{avg} \\ &\text{if } p_g^{avg} > P_o, \text{ then } n_g = \frac{n_g P_c}{p_g^{avg}} \text{ and } p_g^{avg} = P_c \end{aligned} \tag{16}$$

where n_g is the number of moles in gas. All gas partial pressures and their local concentrations decrease accordingly with venting.

4.2. Initial and boundary conditions

To close the mathematical system, initial and boundary conditions for the primary variable are necessary. The potentials in the solid and electrolyte phases are governed by Poisson equation without time derivatives, hence, their initial conditions are not necessary. The appropriate boundary conditions for ϕ_s and ϕ_e are

$$\phi_s = 0 \text{ or } V \tag{17}$$

on the current collectors for a given voltage, or

$$-\sigma_{eff} \frac{\partial \phi_s}{\partial \boldsymbol{n}} = I \tag{18}$$

for a prescribed current density. Everywhere else on the cell boundaries, one has

$$\frac{\partial \phi_e}{\partial \boldsymbol{n}} = \frac{\partial \phi_s}{\partial \boldsymbol{n}} = 0 \tag{19}$$

where $\boldsymbol{n}$ is the unit vector normal to the boundary surface. The concentration initial/boundary conditions are given by

$$c^i = c_0^i, \quad \text{at } t = 0; \qquad \frac{\partial c^i}{\partial \boldsymbol{n}} = 0 \tag{20}$$

The temperature initial/boundary conditions can be written as

$$T = T_0, \quad \text{at } t = 0; \qquad -\lambda_c \frac{\partial T}{\partial \boldsymbol{n}} = h(T - T_a) \tag{21}$$

where λ_c is the thermal conductivity of the case material, and h the overall convective heat coefficient that may include the effects of other heat transfer modes and T_a is the ambient temperature.

The initial conditions for electrolyte velocity and saturation level is determined by assuming that the system is initially at equilibrium, i.e.

$$\boldsymbol{v}_e = 0, \quad \text{at } t = 0 \tag{22}$$

and

$$D_c \nabla s + D_{\varepsilon/K} \nabla \left(\frac{\varepsilon}{K}\right)^{1/2} = 0, \quad \text{at } t = 0 \tag{23}$$

That is, there is no electrolyte flow initially. Electrolyte starts to flow after electrode reactions take place, resulting in changes in volume fractions of solid and electrolyte, and thus, changes in the electrolyte saturation level, porosity, and permeability.

Eq. (23) is used to evaluate the initial electrode permeability given the permeability of separator. At electrode/separator interfaces, there are sharp changes of electrolyte saturation and porosity. Eq. (23) shows that the velocity induced by the saturation gradient is balanced by the velocity caused by the gradient of $(\varepsilon/K)^{1/2}$ at equilibrium.

5. Numerical procedures

To numerically solve the foregoing model equations, the general computational fluid dynamics (CFD) methodology is adopted in the present work. The key to a successful application of CFD techniques is that all the equations in the present battery model can be cast into a general form of convection–diffusion type, i.e.

$$\underset{\text{accumulation}}{\frac{\partial(\varepsilon \Phi)}{\partial t}} + \underset{\text{convention}}{\nabla \cdot (\boldsymbol{v} \Phi)} = \underset{\text{diffusion}}{\nabla \cdot (\Gamma_\Phi \nabla \Phi)} + \underset{\text{source}}{S_\Phi} \tag{24}$$

where Φ is the general variable to be solved, Γ_Φ the diffusion coefficient, and S is the source term which includes all terms that cannot be included in the previous terms.

The general differential equation is then discretized by the control volume-based finite difference method of Patankar [16] and the resulting set of algebraic equations is iteratively solved. The numerical solver for the general differential equation can be repeatedly applied for each scalar variable over a control volume mesh. The solution of each of the components of the electrolyte momentum equation is, however, obtained in a staggered control volume using semi-implicit method for pressure-linked equations revised (SIMPLER) algorithm (see [16] for details). The rectangular physical domain is divided by either a uniform or non-uniform grid consisting of m horizontal and n vertical grid lines. Stringent numerical tests are performed to ensure that the solutions are independent of the grid size and time step. The equations are solved as a simultaneous set, and convergence is considered to be reached when the relative error in each field between two consecutive iterations is less than 10^{-5}.

6. Results and discussion

Fig. 3 compares the model predictions with the experimental data from charging a VRLA cell at $C/10$ with 40% overcharge [4], showing reasonable agreement in predicting both the cell potential and pressure. Specifically, the model successfully captures two key features observed in charging

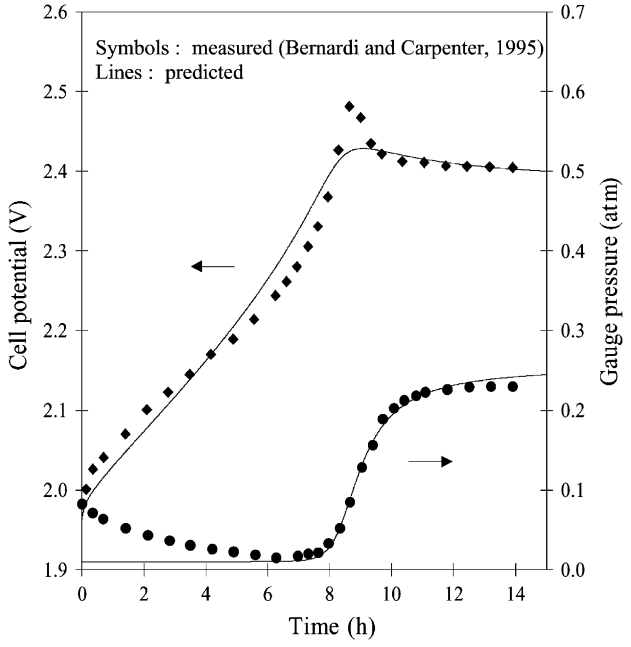

Fig. 3. Comparisons with experimental data.

of a VRLA cell—the potential rollover and pressure stabilization as overcharge proceeds.

In the following figures, the unique capabilities of the present model, namely, (1) simulating oxygen gas transport; (2) venting event and (3) capillary flow, will be illustrated. Numerical simulations are performed to study the effects of important parameters such as the electrolyte saturation level, interfacial mass transfer coefficient of oxygen, and MF of an electrode. The effects of venting event, charging algorithm, and capillary flow are also explored. The simulated battery has a nominal capacity of 70 Ah. It is configured with four cells in series, so its open-circuit voltage is approximately 8.6 V at 100% SOC. In the following studies, the response of the battery charged at a constant current of 25 A (C/2.8) will be explored.

Fig. 4 shows the effect of electrolyte saturation level on the cell performance. Three values of acid saturation level in the separator are considered: 83, 88 and 93%, while 85% acid saturation is assumed for the positive and negative electrodes. Fig. 4 shows that the acid saturation level does not have significant effect on the battery performance until oxygen reactions come into play when approaching overcharge. A smaller value of acid saturation level (i.e. a larger void volume for the gas phase and, hence, larger effective oxygen gas diffusion coefficient) yields a more pronounced potential rollover and a lower stabilized pressure, indicating that oxygen transport from the positive electrode, where it is generated, to the negative electrode, where it is recombined, through the separator indeed plays an important role in the operation of VRLA batteries. The increase in oxygen recombination rate at lower acid saturation has been seen to be important in designing an optimal charging algorithm [3].

The sharp increase in the cell potential at the end of charge occurs when the negative electrode is completely charged and available oxygen is not sufficient to provide a balanced amount of current to that of the positive electrode. Therefore, it is an indication of oxygen mass transport limitation, as reflected by the sequential occurrence of the potential jumps in Fig. 4. This can be further illustrated by Fig. 5, which shows the effect of oxygen transport from the positive to the negative electrode. In Fig. 5, the solid line represents the base case with finite values of the interfacial mass transfer coefficient k and oxygen gas diffusion coefficient $D_g^{O_2}$, and the dashed line stands for the case with infinitely large values of k and $D_g^{O_2}$ (i.e. no mass transfer resistance is present for oxygen). As a result, all oxygen generated in the positive electrode is consumed in the negative electrode. No cell pressure build-up due to the accumulation of oxygen is seen. The reaction currents are always balanced so that the

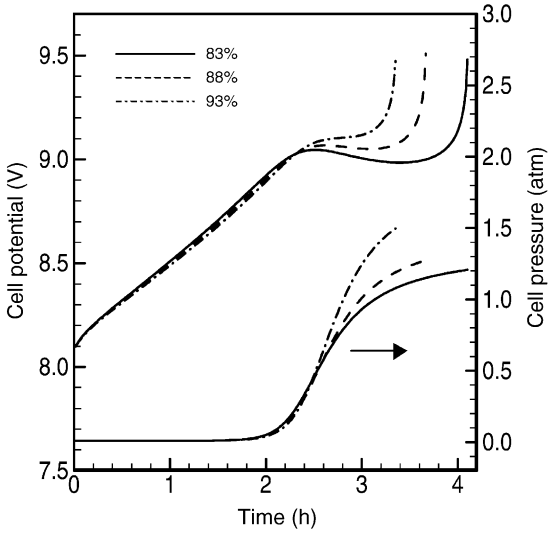

Fig. 4. Effect of electrolyte saturation in the separator.

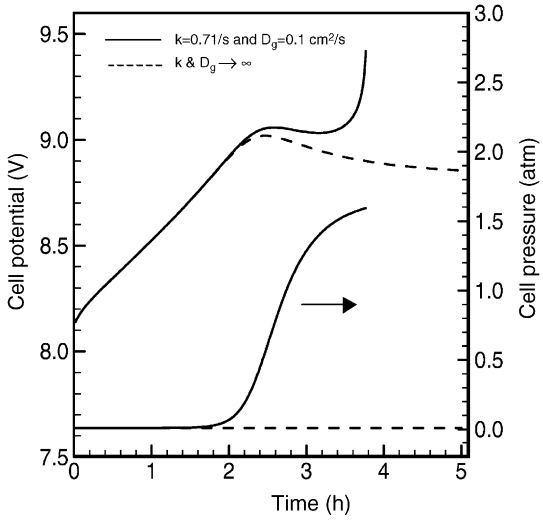

Fig. 5. Effect of oxygen gas transport.

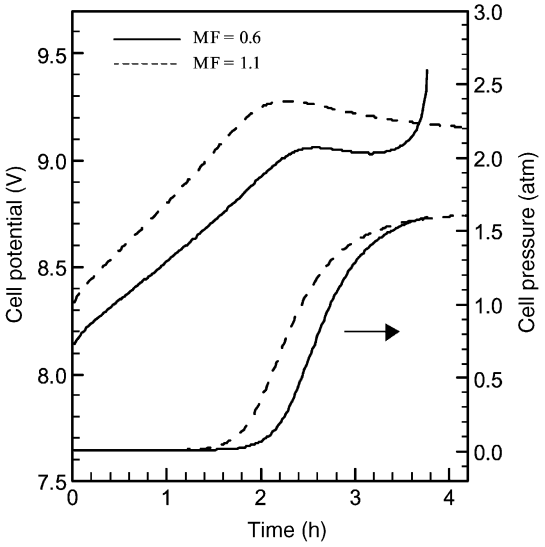

Fig. 6. Effect of MF.

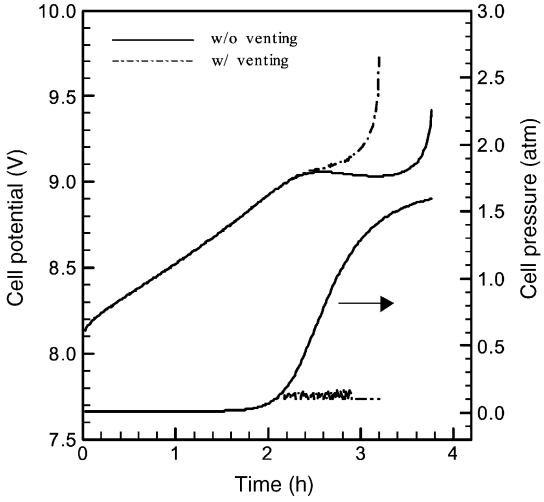

Fig. 7. Effect of venting.

cell potential gradually approaches a constant and no other side reactions come into play. Fig. 5 only gives a combined effect of k and $D_g^{O_2}$. Simulations performed to separate the two effects suggest that while the oxygen transport in the gas phase is greatly affected by the acid saturation level through the effective oxygen gas diffusion coefficient, the interfacial mass transfer of the dissolved oxygen is more crucial to the oxygen recombination in the negative electrode.

Fig. 6 shows the effect of MF that accounts for the passivation effect of $PbSO_4$ on the specific electroactive area, as shown by Eqs. (11) and (12). During charging, a smaller value of MF yields a slower change in the specific area. Consequently, the surface overpotential that drives the electrode reaction is smaller, and the potential of the positive electrode remains comparatively low and, thus, oxygen evolution takes place later. On the other hand, a larger value of MF yields a higher surface overpotential and the oxygen reactions occur earlier and become dominant. As a result, the final jump in the cell potential disappears as the negative electrode has not yet achieved fully-charged state.

Fig. 7 compares the cell performance between cases with and without venting. The valve-opening and closing pressures are 0.17 and 0.10 atm (gauge pressure), respectively. It is shown that with venting the cell pressure is windowed within the preset pressures. The cell potential increases faster with venting due to the faster conversion of $PbSO_4$ to Pb at the negative electrode, as the primary reaction current remains higher when oxygen generated in the positive electrode releases to the ambient and not recombined in the negative electrode to consume a portion of total current.

Fig. 8 shows the effect of hydrogen evolution in the negative electrode on the evolutions of cell potential and pressure. Since hydrogen recombination in the positive electrode is kinetically hindered, hydrogen gas, once generated, immediately contributes to the cell pressure build-up. The cell potential responses to the hydrogen evolution with a large step rise followed by gradual decrease due to oxygen recombination as overcharge proceeds. Fig. 8 also shows the effect of venting in the presence of hydrogen evolution. The difference in the cell potential between cases with and without venting is substantial. In particular, no gradual decrease in the cell potential is seen because significant amount of oxygen generated at the positive electrode is vented rather than recombined at the negative electrode. In other words, oxygen recombination is inefficient, causing hydrogen excursions to remain high. Such behavior of cell potential is unique for the VRLA battery experiencing significant gassing and venting [17].

Fig. 9 displays the temperature evolutions of the battery under various charging algorithms. Three charging algorithms are considered: continuous current (CC), current interrupt (CI), and control charge. The CC charging algorithm involves an initial high rate, followed by a number of step-wise decreased charging rates, and finally a fixed low rate that may be higher than the preceding one. Under CI

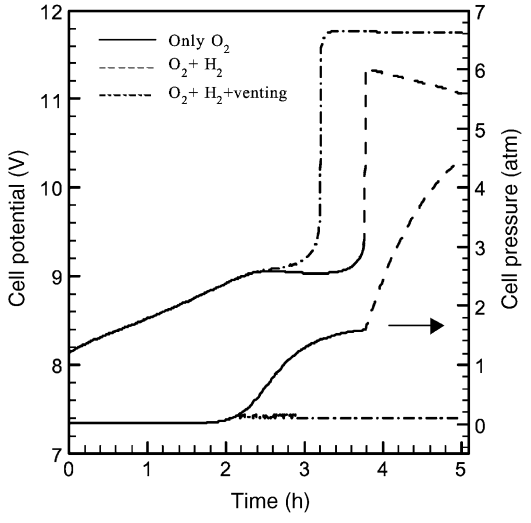

Fig. 8. Effect of hydrogen evolution.

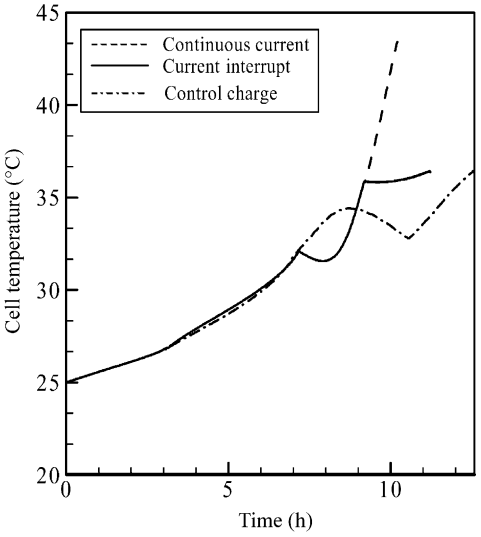

Fig. 9. Effect of charging algorithm on cell temperature.

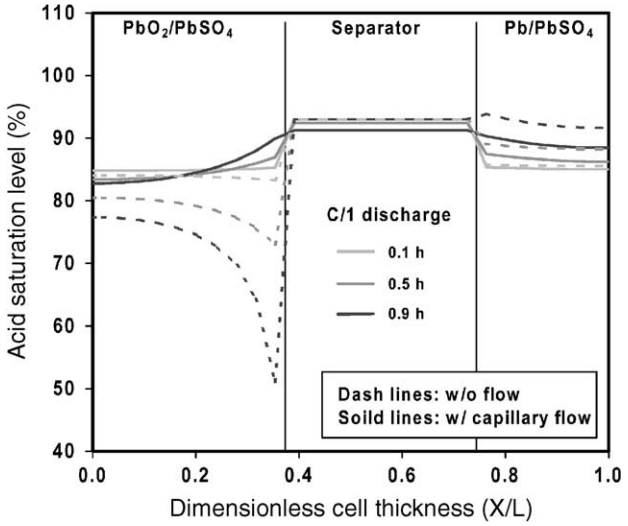

Fig. 11. Effect of capillary flow on the distributions of electrolyte saturation during *C*/1 discharge.

charging algorithm the battery is charged at a nearly constant high rate and then pulse-charged at a relatively low rate near the fully-charged state [3]. The control charge is similar to the CI but more complex.

The battery is exposed to the ambient and is cooled primarily by free air convection. Significant differences in the battery temperature occur during overcharge. Essentially, CC yields a continuous increase in temperature with possibility of thermal runaway at the end of charging. CI caps the temperature below 37 °C and not only achieves full capacity but also ensure safe operation of the battery. The temperature evolution in the control charge process also remains low with longer charging time. The battery experiences a decrease in its temperature in all cases in accordance with the high to low rate transition involved in a charging algorithm. Fig. 9 demonstrates a unique capability of the present thermal-electrochemical coupled model.

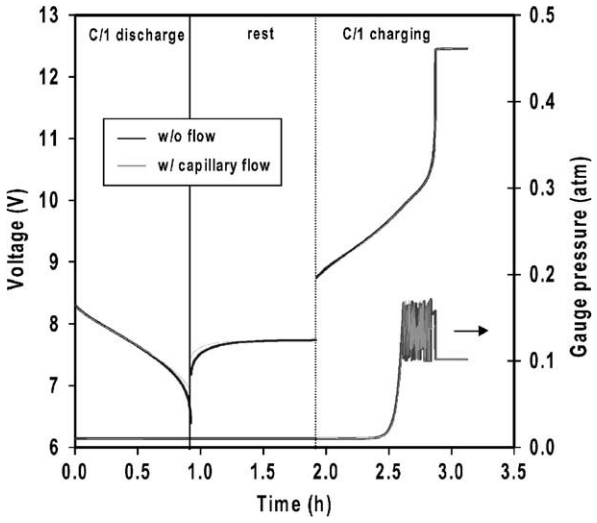

Fig. 10. Effect of capillary flow on the battery voltage and pressure.

Fig. 10 shows the effect of capillary flow on the battery voltage and pressure during a simple discharge/rest/charging cycle. With a preset cut-off voltage, the simulation considering capillary flow yields about 10% more in the discharge capacity, due to the fact that capillary flow enhances the electrolyte supply from the separator to the positive electrode where the electrolyte tends to be depleted during discharge. The difference in cell potential between cases considering and ignoring capillary flow is negligible during charging. The difference in the cell pressure is also small because most changes are masked by the venting events that occur. However, substantial differences in the distributions of acid saturation level are observed from Fig. 11 for discharge and Fig. 12 for charging. While the case considering capillary flow predicts a more even distribution of

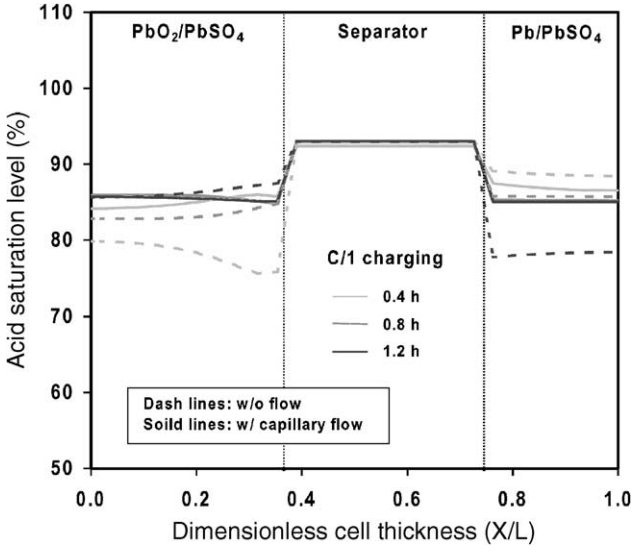

Fig. 12. Effect of capillary flow on the distributions of electrolyte saturation during *C*/1 charging.

acid saturation level which reflects the reality, the case ignoring capillary flow yields highly non-uniform profiles of acid saturation level. These predictions illustrate the importance of including capillary flow in battery models. The effect is expected to be significant in predicting battery cycle life where there are a large number of deep charge/discharge cycles.

7. Conclusion

This paper provides an overview of the simulation capabilities of the present multiphase, electrochemical and thermal coupled model for VRLA batteries. Numerical simulations were carried out to show the effects of the electrolyte saturation level, interfacial mass transfer coefficient of oxygen, MF, venting, charging algorithm, and capillary flow on the battery performance. Accurate estimation of the parameters that govern these phenomena would allow this comprehensive model to be used in designing proper charging algorithms for better performance and cycle life.

Acknowledgements

We would like to greatly acknowledge Dr. Ronald Brost of Ford Motor Company, Dr. Bob Nelson of Recombination Technologies, and Dr. Venkat Srinivasan of Penn State Electrochemical Engine Center for many useful discussions.

Appendix A. Derivation of the momentum equation for capillary flow

Conservation of mass over the liquid phase yields

$$\frac{\partial \varepsilon_e}{\partial t} + \nabla \cdot \boldsymbol{v}_e = S_e^V \tag{A.1}$$

where the term S_e^V represents electrolyte displacement during battery operation resulting from the change in partial molar volumes between the reactants and products. The flow of electrolyte in porous media is usually described by Darcy's law, i.e.

$$\boldsymbol{v}_e = -\frac{Kk_{re}}{\mu}\nabla p_e \tag{A.2}$$

where p_e is the pressure in the electrolyte, K the absolute permeability of the porous medium like electrode and separator, k_{re} the relative permeability of the phase of electrolyte, and μ is the dynamic viscosity of the electrolyte. Since the electrolyte pressure differs from the gas pressure by a capillary pressure [15], namely,

$$p_e = p_g - p_c \tag{A.3}$$

Eq. (A.2) can be rewritten as

$$\boldsymbol{v}_e = \frac{Kk_{re}}{\mu}\nabla p_c - \frac{Kk_{re}}{\mu}\nabla p_g \tag{A.4}$$

The first term on the right-hand side of Eq. (A.4) describes the electrolyte flow driven by capillary forces, whereas the second term represents the electrolyte displacement by the gradient in the gas pressure. The first term is dominant when the thickness of an unsaturated cell is small and as a result, the gas phase pressure is nearly uniform. Neglecting the gradient in gas phase pressure, one has

$$\boldsymbol{v}_e = \frac{Kk_{re}}{\mu}\nabla p_c \tag{A.5}$$

The absolute permeability of a porous medium can be evaluated by the Kozeny–Carman relation

$$K = \frac{\varepsilon^3}{5a_{se}^2} = \frac{\varepsilon^3 d_s^2}{180(1-\varepsilon)^2} \tag{A.6}$$

where ε is the porosity of the porous medium and d_s is the diameter of spherical particles making up it.

The relative permeability of the electrolyte phase is a function of electrolyte saturation [15]

$$k_{re} = s^n \tag{A.7}$$

where the index n is an empirical value varying between 1 and 3.

The two-phase capillary pressure can be expressed in terms of a Leverett function $J(s)$ [15], namely,

$$p_c = \sigma\left(\frac{\varepsilon}{K}\right)^{1/2} J(s) \tag{A.8}$$

Making use of Eqs. (A.6–A.8), and the definition of electrolyte saturation Eq. (8), Eq. (A.5) becomes

$$\boldsymbol{v}_e = -D_c\nabla s - D_{\varepsilon/K}\nabla\left(\frac{\varepsilon}{K}\right)^{1/2} \tag{A.9}$$

where

$$D_c = -\sigma\left(\frac{\varepsilon}{K}\right)^{1/2} J'(s)\frac{Kk_{re}}{\mu} \tag{A.10}$$

and

$$D_{\varepsilon/K} = -\sigma J(s)\frac{Kk_{re}}{\mu} \tag{A.11}$$

D_c represents capillary diffusion coefficient and has a unit of cm^2/s. Substituting Eq. (A.9) into Eq. (A.1), one has

$$\varepsilon\frac{\partial s}{\partial t} = \nabla \cdot D_c\nabla s + \nabla \cdot D_{\varepsilon/K}\nabla\left(\frac{\varepsilon}{K}\right)^{1/2} + (S_e^V + sS_s^V) \tag{A.12}$$

References

[1] R.F. Nelson, J. Power Sources 31 (1990) 3–22.
[2] D. Berndt, Maintenance-free Batteries, Research Studies Press Ltd., 1993.

[3] R.F. Nelson, E.D. Sexton, J.B. Olson, M. Keyser, A. Pesaran, J. Power Sources 88 (2000) 44–52.
[4] D.M. Bernardi, M.K. Carpenter, J. Electrochem. Soc. 142 (1995) 2631–2642.
[5] J. Newman, W. Tiedemann, J. Electrochem. Soc. 144 (1997) 3081–3091.
[6] W.B. Gu, C.Y. Wang, B.Y. Liaw, J. Electrochem. Soc. 144 (1997) 2053–2061.
[7] W.B. Gu, C.Y. Wang, B.Y. Liaw, J. Power Sources 75 (1) (1998) 151–161.
[8] H. Huang, T.V. Nguyen, J. Electrochem. Soc. 144 (1997) 2420–2426.
[9] D. Berndt, U. Teutsch, J. Electrochem. Soc. 143 (1996) 790–798.
[10] C.Y. Wang, W.B. Gu, B.Y. Liaw, J. Electrochem. Soc. 145 (1998) 3407–3417.
[11] W.B. Gu, C.Y. Wang, J. Electrochem. Soc. 147 (2000) 2910–2922.
[12] W.B. Gu, S. Li, C.Y. Wang, M.M. Geng, B.Y. Liaw, Electrochimica. Acta 44 (1999) 4525–4541.
[13] B. Culpin, J.A. Hayman, in: L.J. Pearce (Ed.), Power Sources, Vol. 11, Brighton, England, 1986, pp. 45–66.
[14] R.D. Brost, in: Proceedings of the 15th Annual Battery Conference on Applications and Advances, IEEE, Long Beach, 2000, pp. 243–248.
[15] C.Y. Wang, P. Cheng, in: J.P. Hartnett, et al. (Eds.), Advances in Heat Transfer, Vol. 30, Academic Press, New York, 1997, pp. 93–196.
[16] S.V. Patankar, Numerical Heat Transfer and Fluid Flow, Hemisphere, Washington, DC, 1980.
[17] R. Nelson, J. Metals 1 (2001) 28–33.